ACS NANO

www.acsnano.org

ARTICLE

Uncovering an Interfacial Band Resulting from Orbital Hybridization in Nickelate Heterostructures

Mingyao Chen, Huimin Liu, Xu He, Minjuan Li, Chi Sin Tang,* Mengxia Sun, Krishna Prasad Koirala, Mark E. Bowden, Yangyang Li, Xiongfang Liu, Difan Zhou, Shuo Sun, Mark B.H. Breese, Chuanbing Cai, Le Wang,* Yingge Du, Andrew T. S. Wee, and Xinmao Yin*

Cite This: *ACS Nano* 2024, 18, 27707−27717

Read Online

ACCESS | Metrics & More | Article Recommendations | Supporting Information

ABSTRACT: **The interaction of atomic orbitals at the interface of perovskite oxide heterostructures has been investigated for its profound impact on the band structures and electronic properties, giving rise to unique electronic states and a variety of tunable functionalities. In this study, we conducted an extensive investigation of the optical and electronic properties of epitaxial $NdNiO_3$ synthesized on a series of single-crystal substrates. Unlike nanofilms synthesized on other substrates, $NdNiO_3$ on $SrTiO_3$ (NNO/STO) gives rise to a unique band structure featuring an additional unoccupied band situated above the Fermi level. Our comprehensive investigation, which incorporated a wide array of experimental techniques and density functional theory calculations, revealed that the emergence of the interfacial band structure is primarily driven by orbital hybridization between the Ti 3d orbitals of the STO substrate and the O 2p orbitals of the NNO thin film. Furthermore, exciton peaks have been detected in the optical spectra of the NNO/STO film, attributable to the pronounced electron−electron (e−e) and electron−hole (e−h) interactions propagating from the STO substrate into the NNO film. These findings underscore the substantial influence of interfacial orbital hybridization on the electronic structure of oxide thin films, thereby offering key insights into tuning their interfacial properties.**

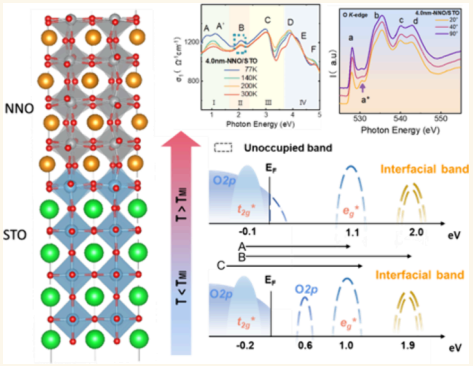

KEYWORDS: *oxide heterostructures, interfacial orbital hybridization, excitonic propagation, spectroscopic ellipsometry, X-ray absorption spectroscopy, density functional theory*

INTRODUCTION

Strongly correlated oxide systems have emerged as a central focus in the realm of condensed matter physics, largely due to the complex many-body interactions inherent within these systems.[1,2] Interfaces in oxides, with unique structural characteristics, offer a platform for exploring unique phenomena not observable in bulk materials.[3,4] Moreover, significant advances in device technology have underscored the significance of interfaces in these materials,[5,6] emphasizing their pivotal role in leveraging the unique properties of strongly correlated oxides within this field.

Interfacial electronic states can undergo significant modifications due to effects induced by orbital hybridization, lattice mismatches, and charge transfer. In first-row transition metal oxides, the hybridization between the 3d band of the transition metal component and the 2p bands of the oxygen component significantly influences their electronic and band properties. Previous studies have emphasized the crucial role of interfacial hybridization in governing charge transfer dynamics between nickelates and other perovskite oxides,[7−9] as well as its impact on charge localization in copper-based high-temperature superconductors.[10] In addition, interfacial hybridization has been observed to significantly affect the magnetic properties,[11−15] leading to a variety of other quantum effects.[16−18] Therefore, elucidating the mechanism and effects of interfacial orbital hybridization is essential for a more thorough and comprehensive understanding of the material properties.

However, the investigation of specific impacts of the interface within oxide heterostructures at the nanoscale

Received: July 23, 2024
Revised: September 12, 2024
Accepted: September 17, 2024
Published: September 26, 2024

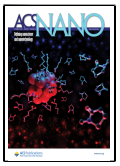

remains challenging due to their complex nature and diverse structure variations. In addressing this challenge, perovskite oxide systems, characterized by their unique structural and electronic features, offer an ideal platform for such inquiries.[19−21] The rotational and distortive dynamics of oxygen octahedra in perovskite oxides play a crucial role in inducing asymmetry at the oxide/substrate interface. This asymmetry, in turn, influences the spin−orbit coupling and gives rise to various interfacial phenomena.[22−24] Among the perovskite oxide materials, rare earth nickelates ($RNiO_3$, where R denotes the lanthanide atom) have attracted increasing attention for their intriguing electronic properties and the emergence of superconductivity.[25−27] The structural and physical properties of nickelates can be modified by adjusting and varying the types of rare earth element.[28−31] Interestingly, they can be further manipulated by the use of substrate effects via the onset of interfacial interactions at the film−substrate interface. A case in point is the $SrTiO_3$ (STO) class of materials in which high-energy resonant excitons have been reported,[32] and they are reported to interact strongly with thin-film layers such as graphene, manganite film, cuprate superconductors, and 2D materials via an intricate series of interfacial interactions. These effects have a direct impact on the electronic and optical properties of these materials.[33−36] Such studies provide an imperative to introduce and manipulate the propagation of excitons from 3D STO substrate materials to thin-film structures.[37] Furthermore, extensive studies on the interfacial effects of nickelates have unveiled intriguing phenomena absent in bulk materials.[38−42]

In this study, we employed spectroscopic techniques to probe the interfacial electronic structure of $NdNiO_3$ films grown on different substrates. Our comprehensive experimental approach, including temperature-dependent spectroscopic ellipsometry and X-ray absorption spectroscopy (XAS), yielded a detailed understanding of the optical spectra associated with these heterostructures. Our results reveal clear changes in electronic structures when varying the substrate, including the appearance of a new high-energy state and the detection of exciton peaks. Detailed density functional theory (DFT) calculations further support our experimental findings, revealing a strong hybridization effect between Ti 3d orbitals of the STO substrates and O 2p orbitals of the NNO film at the NNO/STO interface. This intricate interfacial hybridization process critically contributes to the radical changes observed in the electronic structures of the NNO film. These findings highlight the significance of interfacial orbital hybridization, offering valuable methodologies and insights into investigating the interfacial effects in complex oxide heterostructures.

RESULTS AND DISCUSSION

Synthesis and Characterization of NNO Films. High-quality epitaxial NNO thin films with thicknesses between 4.0 and 12.0 nm were deposited on (001)-oriented $LaAlO_3$ (LAO), $(LaAlO_3)_{0.3}(Sr_2AlTaO_6)_{0.7}$ (LSAT), and STO substrates by using pulsed laser deposition (PLD). NNO possesses an orthorhombic crystal structure with a pseudo-cubic room-temperature lattice constant of ∼3.81 Å in its bulk form,[43,44] which is larger than that of the LAO substrate (a_{LAO} ≈ 3.793 Å), but smaller than those of LSAT (a_{LSAT} ≈ 3.868 Å) and STO (a_{STO} ≈ 3.905 Å) substrates. Hence, the NNO film experiences a compressive strain of ∼−0.47% when deposited on LAO and a tensile strain of 1.52% (2.49%) when grown on the LSAT (STO) substrate, as shown in Figure 1a. Figure 1b displays the X-ray diffraction (XRD) θ-2θ scans near the (001)

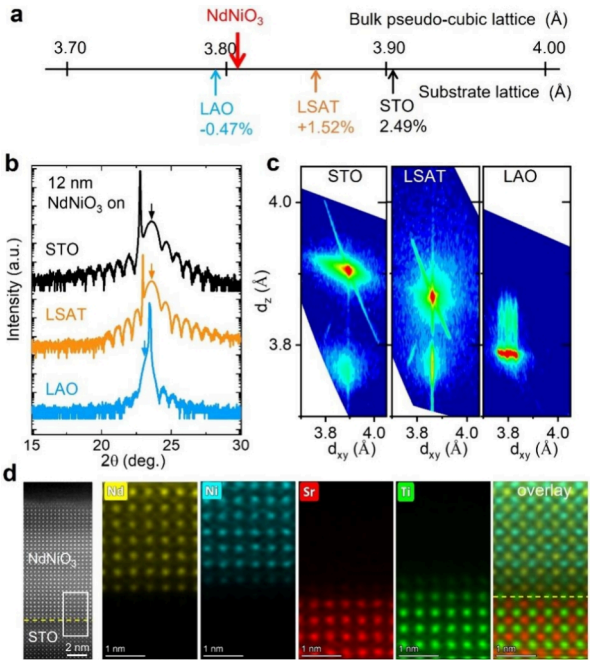

Figure 1. Synthesis of NNO films and structural characterization. (a) Lattice mismatch between bulk NNO and the substrates used in this study. (b) XRD θ−2θ scans near the (001) peak of NNO films on STO, LSAT, and LAO substrates. NNO films peaks are marked by arrows. (c) Reciprocal space mapping (RSM) for 12.0 nm-thick NNO on STO, LSAT, and LAO substrates. (d) Cross-sectional STEM image (left) of the NNO/STO interface viewed along the [100]-direction of STO. Atomic-resolution EDS mapping (right) of the NNO/STO interface. Yellow, blue, red, and green respectively represent the Nd, Ni, Sr, and Ti atoms.

peaks for the representative 12.0 nm NNO films. The strain effect induces a notable change in the out-of-plane lattice parameter of NNO films, as evidenced by the peak shift to higher 2θ angle when transitioning from LAO to STO. The distinct thickness fringes around the Bragg peaks indicate the high-quality NNO films. Reciprocal space maps (RSMs) (Figure 1c) near the (103) reflection confirm that the 12.0 nm-thick NNO films are coherently strained to the substrates. Figure 1d presents a high-angle annular dark-field scanning transmission electron microscopy (HAADF-STEM) image of the 12 nm NNO film on STO. This image shows the good quality of the sample and reveals the absence of apparent structural defects, such as Ruddlesden−Popper phases and NiO secondary phases, within the NNO film. Furthermore, atomic-resolution energy-dispersive X-ray spectroscopy (EDS) maps were conducted to unveil the chemical distribution across the NNO/STO interface. The EDS maps for Nd (yellow), Ni (blue), Sr (red), and Ti (green) elements are presented individually. A superimposed overlay of these maps confirms a stacking sequence of $NiO_2/NdO/TiO_2/SrO$ at the interface, with some Ti/Ni intermixing due to Ti out-diffusion. This observation aligns with recent findings regarding the polar interface of infinite-layer nickelate thin films.[45]

Electrical Transport Properties and Optical Conductivity Spectra of NNO Films. Figure 2a shows the temperature-dependent resistivity of NNO films grown on an

https://doi.org/10.1021/acsnano.4c09921
ACS Nano 2024, 18, 27707−27717

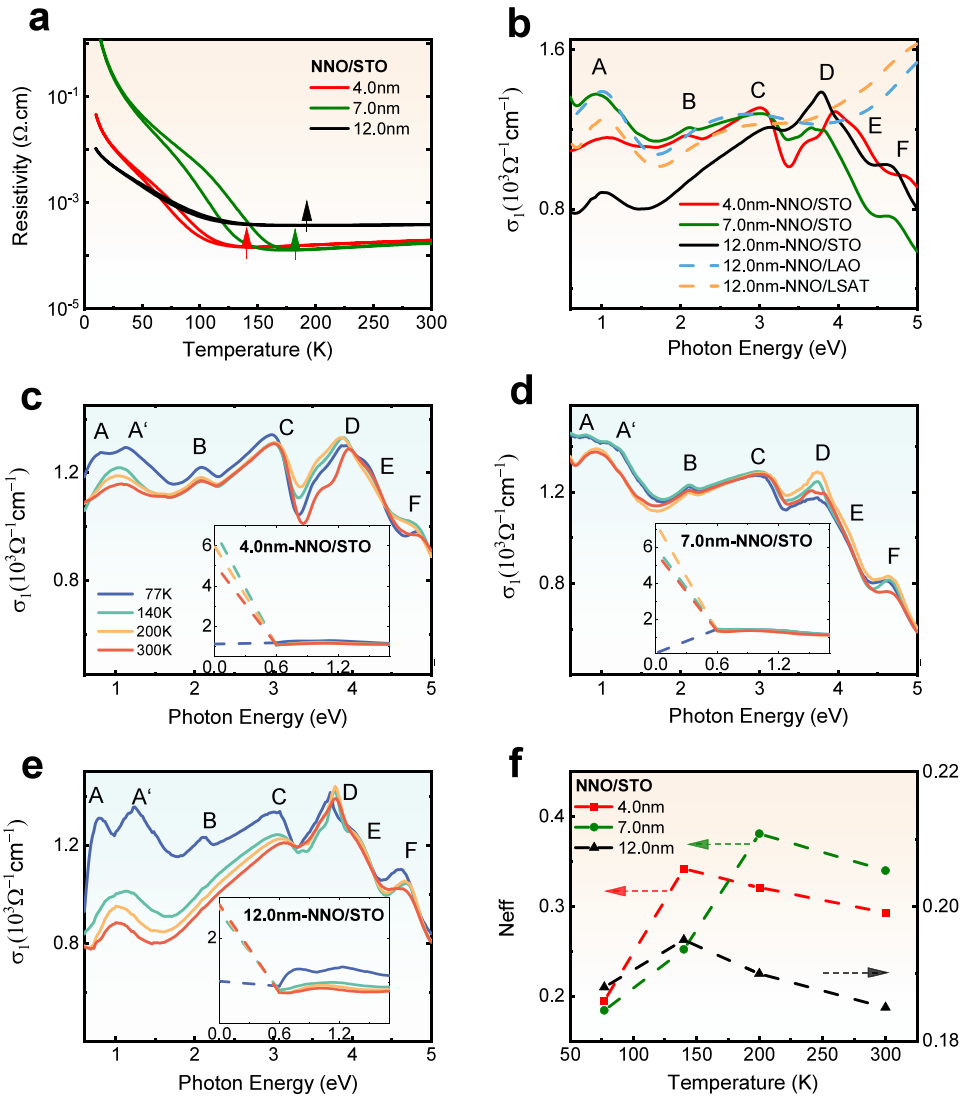

Figure 2. Temperature-dependent electrical and optical properties of NNO films. (a) Temperature-dependent resistivity of the NNO/STO samples with different film thicknesses. The inset shows the 12.0 nm-thick NNO films on various substrates. Arrows indicate the temperature at which metal−insulator transition takes place in each thin-film sample. (b) Room-temperature optical conductivity, σ_1, of the respective NNO films. Temperature-dependent σ_1 spectra of (c) 4.0 nm-, (d) 7.0 nm-, and (e) 12.0 nm-thick NNO films grown on STO at temperatures ranging from 77 to 300 K. The insets in (c−e) are the temperature-dependent σ1 spectra for 0−1.7 eV of respective NNO/STO thin films. The σ_1 at photon energies between 0 and 0.6 eV displayed as dashed lines of the respective colors is estimated using a linear interpolation (σ_1 at 0 eV is estimated from the DC conductivity in Figure 2a). (f) Number of effective charges (N_{eff}) as a function of temperature for 0−1.7 eV.

STO with varying thicknesses. With increasing the NNO film thickness from 4.0 to 12.0 nm, T_{MI} gradually rises and approaches the bulk value of 200 K. However, for the 12.0 nm NNO films, there is a prominent increase in the resistivity value, and the metal−insulator transition process appears less distinctive. This behavior could be attributed to the presence of oxygen vacancies, possibly induced by the larger tensile strain effect.[46−48] The temperature-dependent resistivity of the NNO films on other substrates is shown in Supporting Information Figure S1. Further analysis of the carrier dynamics was based on our optical measurements derived from the spectroscopic ellipsometry, as discussed in greater detail thereafter.

The distinctive electrical transport properties of NNO films on different substrates and with different thicknesses are readily reflected in the outcomes of the optical conductivity $\sigma_1(\omega)$ (Figure 2b), which have been derived from comprehensive spectroscopic ellipsometry measurements. The σ_1 spectra of all NNO films exhibit common features including a peak *A* at ∼1.24 eV and a broad optical feature *C* at ∼3.05 eV. Based on the previous reports, peak *A* is associated with the optical transition between occupied and unoccupied antibonding e_g* orbitals,[49,50] while feature *C* arises from the transition between the O 2p orbital and the unoccupied e_g* band.[49] The σ_1 spectra of both NNO/LAO and NNO/LSAT are in line with previous reports,[51−54] while the spectra of NNO/STO exhibit notable deviations in optical characteristics that have yet to be explained. In particular, the emergence of features *B* (∼2.12 eV), *D* (∼3.75 eV), *E* (∼4.10 eV), and *F* (∼4.67 eV) require further scrutiny in order to elucidate their origins.

https://doi.org/10.1021/acsnano.4c09921
ACS Nano 2024, 18, 27707−27717

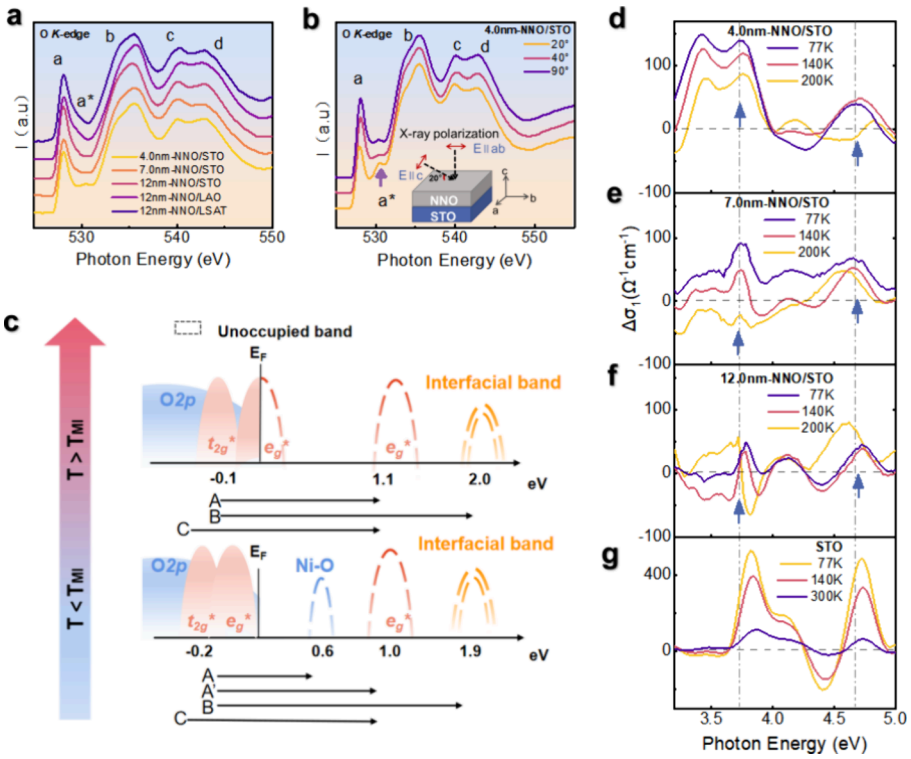

Figure 3. O *K*-edge XAS of NNO film samples and energy band schematics. (a) O *K*-edge XAS of the NNO film samples. (b) Polarization-dependent O *K*-edge XAS of the 4.0 nm-thick NNO/STO sample. (c) Energy band schematic of the 4.0 nm-thick NNO/STO sample in the high-temperature metallic state (top) and low-temperature insulating state (bottom). Differential optical conductivity, $\Delta\sigma_1$ (where $\Delta\sigma_1(\omega,T) = \sigma_1(\omega,T) - \sigma_1(\omega,300\ \mathrm{K})$), of (d) 4.0 nm NNO/STO, (e) 7.0 nm NNO/STO, and (f) 12.0 nm NNO/STO, and in comparison with the (g) bare STO substrate.

To uncover the origins of these unique optical features in the NNO/STO films, we conducted temperature-dependent ellipsometry measurements. Figure 2c–e displays the combination of temperature-dependent σ_1 spectra (between 0.6 and 5 eV) and transport measurements (0 eV) of NNO/STO samples with varying NNO film thickness. There is a clear temperature-dependent trend in the σ_1 spectra, particularly in the 0–0.6 eV energy region, which have been estimated using linear interpolation[55,56] (where σ_1 at 0 eV is estimated from the DC conductivity in Figure 2a). For all NNO/STO samples, there are two distinct peak features labeled *A* (~0.78 eV) and *A*′ (~1.24 eV) in the σ_1 spectra measured at 77 K. These low-temperature optical features can be attributed to the onset of bond disproportionation in the low-temperature insulating phase.[54,57] As the temperature increases and the insulator-to-metal transition occurs, these two-peak features merge into a single peak. The prominent feature *B* (located at ~2.12 eV) observed in the 4.0 and 7.0 nm NNO/STO samples, absent for NNO films grown on LAO and LSAT (Figure 2b), persists throughout the entire temperature range from 77 and 300 K (Figure 2c,d). Specifically, as the film thickness continues to increase, feature *B* becomes visible only at 77 K in the 12.0 nm-thick NNO/STO sample (Figure 2e) and this feature is suppressed at higher temperatures. The progressive suppression of feature *B* with increasing NNO thickness implies that it is specific to NNO/STO and likely is attributed to interfacial effects that occur at the NNO/STO interface. Further proofs of these interfacial effects can be deduced, as discussed thereafter in the analysis of the XAS results.

In the context of higher photon energy (above ~3.5 eV), the σ_1 spectra of the NNO/STO samples at different film thicknesses reveal two optical features, which are denoted as *D* (~3.75 eV) and *F* (~4.67 eV). Additionally, between features *D* and *F*, an optical shoulder labeled *E* (~4.10 eV) can also be observed. Subsequent discussions and analyses will attribute these optical features to the presence of resonant excitonic effects that originate from the STO substrate.[58]

Having analyzed the σ_1 spectra, we proceed to discuss the variations in the free carrier concentration, N_{eff}, caused by the spectral weight. The metal–insulator transition can also be assessed by the comparison of N_{eff} for different temperatures. To estimate this quantity, we supplemented the optical conductivity with estimated quantities in the photon energy region between 0 and 0.6 eV with transport measurements by conducting a series of linear interpolations (see inset of Figure 2c–e). As it can be observed, for the NNO/STO samples of 4.0 and 7.0 nm, N_{eff} increases marginally with decreasing temperature at high temperatures, this increasing trend continues until the temperature goes below T_{MI} (Figure 2f). Subsequently, a significant decrease in N_{eff} occurs due to the formation of the energy gap associated with the metal–insulator (MI) transition. For the 12.0 nm NNO/STO sample, we can also determine the temperature range in which the metal insulation transition occurs. Therefore, the analysis of N_{eff} is consistent with our transport measurements (Figure 2a).

Electronic States of NNO Films as Revealed by XAS. To precisely determine the origin of the optical features observed in NNO/STO and to further analyze their temperature- and thickness-dependent behavior, we conducted O *K*-edge and Ni *L*-edge XAS for the respective samples. Figure 3a compares the XAS spectra at the *K*-edge of the ohmic rays (O 1s—2p transition) of the respective NNO films.

https://doi.org/10.1021/acsnano.4c09921
ACS Nano 2024, 18, 27707–27717

The prominent pre-edge feature labeled *a*, present in all NNO films at ∼528.1 eV, can be attributed to the Ni 3d—O 2p orbital hybridization, as reported in previous studies.[29,59,60] The broad and resonant feature labeled *b* at a higher energy position of ∼535.4 eV is ascribed to the orbital hybridization between Nd 5d/4f and O 2p orbitals.[61−63] At an even higher photon energy region from ∼537 to 547 eV, features *c* and *d* correspond to the hybridization between the Ni 4sp/Nd 5sp and O 2p orbitals.[61−63] While the origins of majority of the *K*-edge absorption features could be identified, it is crucial to note that a unique small absorption feature labeled *a** at ∼530.5 eV is only present in the NNO/STO samples and absent from NNO films on other substrates. In particular, feature *a** is notably pronounced in the thinnest 4.0 nm NNO/STO sample among all the NNO/STO films. This observation suggests the existence of a new unoccupied hybridized state (with O 1s) that takes place at the NNO/STO interface. Interestingly, the intensity of feature *a** (Figure 3a,b) exhibits a thickness-dependent trend, and this trend mirrors that of optical feature *B* in the σ_1 spectra of NNO/STO samples with varying thicknesses that has been detected using spectroscopic ellipsometry (Figure 2e). The consistent thickness-dependent behavior observed in these two distinct experimental techniques leads to the deduction that features *a** and *B* likely share the same origin that is attributed to the interfacial effects between the NNO film and the STO substrate.

In previous studies involving heterointerfaces with STO as the substrate, optical features similar to what we have observed as *a** were linked to the interfacial hybridization between the Ti 3d orbital belonging to the STO substrate and the O 2p orbital belonging to the respective oxide thin film.[7,12,64] To further substantiate our claim that there is an onset of interfacial hybridization at the NNO/STO interface, particularly in the case of the 4.0 nm NNO/STO sample, we conducted polarization-dependent *K*-edge spectral measurements. Figure 3b displays the intensity variation of the O *K*-edge at 20° (out-of-plane E-field), 90° (in-plane E-field) polarizations, and at an intermediate angle of 40° (inset of Figure 3b). Notably, the intensity of feature *a** is maximized at the 20° (out-of-plane) polarization, while it weakens with increasing polarization angle. The reduced absorption intensity for the in-plane polarization spectra suggests a higher density of out-of-plane empty states, thereby suggesting a stronger out-of-plane orbital hybridization between the Ti 3d orbital of the STO substrate and the O 2p orbital of the NNO film taking place at the film−substrate interface.

Ni *L*-edge XAS measurements were also conducted for the NNO/STO samples of varying film thicknesses (see Supporting Information Figure S7). The shape and peak positions of both the L_3 and L_2 edges remain generally unchanged.[65−67] These features correspond to the Ni 2p → 3d transition[38,61] that are present in Ni electronic states. To further confirm that the XAS measurements probe the interfacial effects at the NNO/STO interface, Ni *L*-edge XAS of the 12.0 and 14.0 nm NNO/LAO samples have also been measured (see Supporting Information Figure S8). In addition to the Ni $L_{3,2}$ edges attributed to the NNO layer, an additional prominent feature is observed at ∼850 eV for the 12.0 nm NNO/LAO sample and it can be ascribed to the La M_4-edge feature belonging to the LAO substrate.[43,66] However, this feature is no longer visible in the 14.0 nm NNO/LAO sample, thereby indicating that the probing depth of the soft XAS technique is between ∼12.0 and 14.0 nm. When considered as a whole, these findings suggest that the XAS characterization for the 4.0, 7.0, and 12.0 nm NNO/STO samples do include signals from their respective interfaces where the underlying hybridization between the STO substrate and NNO film takes place. Thus, the observed feature *a**, notably prominent in the 4.0 nm-thick NNO/STO sample and diminishing with increasing the NNO film thickness, can be attributed to the existence of interfacial orbital hybridization at the NNO/STO interface. Meanwhile, atomic-resolution energy-dispersive X-ray spectroscopy (EDS) maps (Figure 1d) have also confirmed this conclusion; the atomic mixing detected at the interface is known to play a role in enhancing the hybridization between the atomic orbitals.[68]

Electronic Band Diagram and Interfacial Effects of STO on NNO Film. A combined analysis of both the XAS spectra and the σ_1 spectra enables us to construct an electronic band model for the 4.0 nm-thick NNO/STO sample in both metallic and insulating phases. The electronic band model schematic in Figure 3c illustrates the unoccupied bands corresponding to the resonant absorption peaks observed in the *K*-edge O *K*-edge spectra (Figure 3a,b). The energy differences for each band are derived from the peak positions in the optical conductivity spectra.[55] Since the XAS spectra are acquired at room temperature, they reflect the electronic structures in the high-temperature metallic state (top panel of Figure 3c).

The prepeak of the O *K*-edge spectra consists of two distinct features: peak *a* (∼528.1 eV) and a relatively weaker shoulder feature at 529.2 eV. The broad peak feature *a* in the XAS spectra can be attributed to the e_g* and O 2p unoccupied state. Above the Fermi surface, the unoccupied e_g* band close to the unoccupied segment of the e_g* and the O 2p band manifests itself as the shoulder above peak *a* in the O *K*-edge spectra.

As highlighted previously, feature *a** is located at an energy position ∼2.5 eV above peak *a* (Figure 3a) where it corresponds to a previously unidentified unoccupied hybridized state at the same energy position above the Fermi surface. We can attribute the formation of this hybridized state to the robust Ti 3d—O 2p orbital hybridization at the interface between the O 2p orbitals belonging to the NNO film and the Ti 3d orbitals belonging to the STO substrate. Meanwhile, when considering feature B in the σ_1 spectra of the NNO/STO films (Figure 2b) alongside feature *a** of the O *K*-edge spectra, feature B can now be deduced to be corresponding to the optical transition from Ni 3dt_{2g}* bands to the newly formed unoccupied hybridized state *a** registered by the XAS measurement. It is important to note a slight energy mismatch between the ellipsometry (∼2.12 eV) and XAS data (∼2.6 eV), which can be attributed to differences in spectral resolution between these two experimental techniques.

Having established the schematic band diagram for the metallic phase of the 4.0 nm-thick NNO/STO sample, we can extend our analysis to the system's low-temperature insulating state using the σ_1 spectra at 77 K, where features *A* and *A*′ emerge (Figure 2c−e). This emergence can be attributed to the onset of bond disproportionation in the low-temperature insulating phase,[54,57] resulting in the split of the Ni−O hybridized band. Based on the separation distance between features *A* and *A*′, we can assign the unfilled segment of the Ni−O hybridized band to be located ∼0.6 eV above the Fermi energy (bottom panel Figure 3c).

https://doi.org/10.1021/acsnano.4c09921
ACS Nano 2024, 18, 27707−27717

Having established the band diagram of the 4.0 nm NNO/STO based on the spectroscopic ellipsometry and XAS data and combining the results with detailed analysis, it can be seen more intuitively that the interfacial orbital hybridization between the Ti 3d belonging to the STO substrate and the O 2p orbitals of the NNO film results in the formation of the new unoccupied state above the Fermi surface, which is manifested as peak *a** in the O *K*-edge XAS spectra.

Excitonic Effects from the STO Substrate. To further understand the excitonic effects originating from the STO substrate and verify the existence of Ti 3d−O 2p hybridization at the NNO/STO interface, a temperature-dependent differential σ_1, denoted as $\Delta\sigma_1$ (where $\Delta\sigma_1(\omega,T) = \sigma_1(\omega,T) - \sigma_1(\omega,300\ \mathrm{K})$), analysis has been conducted for NNO/STO samples with varying NNO film thicknesses in the high photon energy regions above 3.5 eV (Figure 3d−f). These regions have been previously reported for exhibiting significant effects on thin films due to resonant excitons from the STO substrate.[58,69] In the $\Delta\sigma_1$ spectra, two visible temperature-dependent optical structures located at ∼3.75 and ∼4.67 eV have been observed across all NNO/STO samples. Interestingly, the photon energy positions of these two optical structures are in agreement with the position of two exciton peaks that were observed on bulk STO (Figure 3g)[35] and these peaks have been previously identified as Wannier and resonant excitons, respectively.[58] Furthermore, these features exhibit a similar temperature-dependent behavior as that which has been observed in bulk STO—in particular, its intensity diminishes significantly with increasing temperature. As previous studies have suggested that excitonic wave functions can propagate from the STO substrate to the thin film via interfacial orbital hybridization,[10,34,35] our experimental results indicate the extension and propagation of these excitonic properties from the STO substrate into the NNO film.

While a similar temperature-dependent trend persists with increasing NNO film thickness, the excitonic features observed in the $\Delta\sigma_1$ for both 7.0 and 12.0 nm-thick NNO/STO samples gradually diminish, as seen in Figure 3e,f. This consistency aligns with the experimental observation in the σ_1 spectra for the NNO/STO samples at respective thicknesses, where peaks *D* and *F* are located (Figure 2c−e). Meanwhile, the $\Delta\sigma_1$ spectra for the 12.0 nm NNO/LSAT sample displayed minimal temperature-dependent behavior. This discrepancy allows us to dismiss the notion that the formation of the high-energy optical feature is solely due to lattice strain effects. The presence of optical features within the photon energy range between ∼3.6 and 4.7 eV in the NNO/STO samples underscores the significant impact of the STO substrate on the NNO film, attributed to the intrinsic electron−electron (e−e) and electron−hole (e−h) interactions within the system.

DFT Results of the NNO/STO Interface. To further investigate the interfacial interaction between the NNO film and the STO substrate and its substantial impact on the electronic and optical structures of the NNO/STO sample, first-principles DFT calculations are conducted with the results displayed in Figure 4a.[70−73] Figure 4b−e displays the partial density of states (PDOS) of the Ti, O, and Ni components at the NNO/STO interface, while the hybridized states between O 2p and the Ni/Ti 3d orbitals are schematically illustrated in Figure 4f. When considering the presence of charge ordering in the NNO layer, two types of Ni ions emerge, where they are characterized by the formal oxidation states of Ni^{2+} and Ni^{4+}.

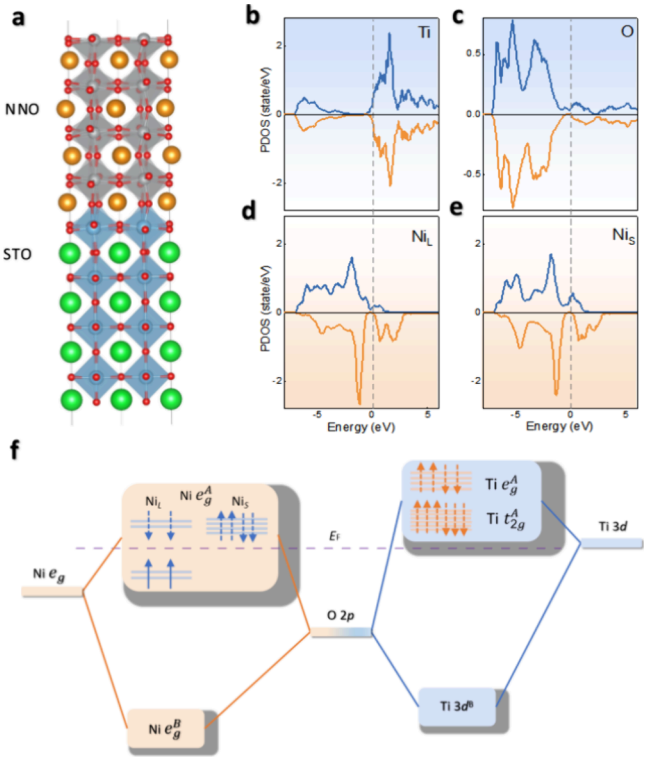

Figure 4. Density functional theory calculations and schematic modeling of the electronic states. (a) NNO/STO superlattice structure modeled for the density of states projected to the (b) Ti, (c) O, and (d) Ni_L, and (e) Ni_S atoms at the interface layers in the phase with Ni−O octahedral breathing distortion. (f) The schematic figure of the hybridization between the Ni, O, and Ti orbitals. The Ni t_{2g} orbitals have not been shown for simplicity. The detailed energy splitting of the bonding state of the Ni e_g and O 2p orbitals and the bonding state between Ti 3d and O 2p orbitals have been displayed. Meanwhile, the other states are shown only in nondetailed way. Superscripts *A* and *B* labels indicate the antibonding and bonding states, respectively.

These two types of Ni ions correspond to a set of larger and a set of smaller Ni−O octahedra sizes, labeled as Ni_L and Ni_S, respectively. The e_g orbitals of the Ni_L ions are occupied by two electrons with two empty states that are separated by a Mott−Hubbard gap. As for the case of the Ni_S ions, the antibonding O 2p e_g orbitals are unoccupied. The difference in the energy gap between the Ni_L and Ni_S ions indicates a site-selective Mott transition.[74] It is noteworthy that the spin polarization for the Ni_S ions (Figure 4e) vanishes in the *S*-type antiferromagnetic structure.[75] These e_g^A (where *A* represents antibonding states) states are located in the energy region of ∼0−3 eV. The interfacial Ti 3d states show significant DOS in the energy region between ∼3 and 5 eV (Figure 4b). Moreover, the O 2p states also has a dominant contribution to the DOS between ∼3 and 5 eV (Figure 4c) while they are absent from the Ni 3d PDOS (Figure 4d,e). The dominant presence of both the Ti 3d and O 2p states is therefore a clear indication of the presence of strong O 2p−Ti 3d orbital hybridization. Its presence leads to the formation of an interfacial state in this energy region. Thus, this phenomenon accounts for the appearance of feature B in the optical spectra detected by using spectroscopic ellipsometry, an optical feature unique to the NNO/STO films that is consistently present throughout the entire temperature range (Figures 2c—e).

https://doi.org/10.1021/acsnano.4c09921
ACS Nano 2024, 18, 27707−27717

While a strong interaction is observed between the NNO film and the STO substrate, such a phenomenon is not replicated in the case of NNO on other substrates. For instance, in the case of NNO/LAO, where the Al 3p orbitals are situated at a relatively higher energy level, the interfacial hybridization between Al 3p and O 2p is significantly weaker, rendering any effects less detectable (see Supporting Information Figure S9). This is also the reason why optical feature *B* (Figure 2b) is absent for NNO films grown on other substrates.

CONCLUSIONS

In conclusion, our observations indicate that NNO thin films grown on STO substrates exhibit a distinctive band structure compared with films grown on other substrates. This distinctiveness is characterized by an additional unoccupied band located above the Fermi level. Through a comprehensive investigation using temperature-dependent spectroscopy ellipsometry, X-ray linear dichroism, and DFT calculations, we have determined that this extra unoccupied band in the NNO/STO samples results from interfacial orbital hybridization between the Ti 3d orbitals of the STO substrate and the O 2p orbitals of the NNO film. These findings underscore the significance of atomic orbital hybridization at oxide interfaces, providing valuable insights into the effects of these interfaces. The ability to design interfacial structures and manipulate atomic orbital interactions not only advances our fundamental understanding of complex oxide heterostructures but also presents exciting opportunities for controlling the electronic structure of materials. Such control holds promising implications for various applications ranging from electronic devices to energy storage systems.

METHODS

Sample Preparation and Characterization. NNO films with thicknesses varying from 4 to 12 nm were deposited on diverse (001)-oriented single-crystal substrates using PLD. Throughout the deposition process, the substrate was held at 675 °C, with an oxygen partial pressure of 300 mTorr. The 248 nm laser fluence was ∼2 J/cm^2, operating at a repetition rate of 5 Hz. After deposition, the oxygen partial pressure was increased to 10 kPa, and the samples were cooled to room temperature at a ramping rate of 25 °C/min. High-resolution XRD measurements were conducted with a Rigaku SmartLab XE instrument equipped with a rotating anode Cu Kα source, a Ge (220) 2-bounce incident monochromator, and a HyPix-3000 two-dimensional detector. The analysis of structural and chemical composition involved HAADF imaging and EDS within a STEM. To prepare the TEM sample, a dual-beam Helios instrument was employed, which combines both focused ion beam (FIB) and scanning electron microscopy (SEM). Initially, a cross-sectional lamella was extracted from the thin film sample through FIB milling, gradually thinning it to approximately 200 nm at 30 kV. The sample was further reduced to about 50 nm at 5 kV before its final polishing at 2 kV. For HAADF imaging, a Thermo Fisher Scientific Spectra Ultra S/TEM equipped with an aberration corrector and a monochromator was used, with a convergence angle of 30 mrad and a collection angle ranging from 60 to 180 mrad. Atomic-scale EDS acquisition and analysis was performed using an advanced EDS detector (Ultra-X) within the STEM with a solid angle of 4.45 srad and operating at a probe current of 42 pA in Velox software. In-plane transport measurements were performed using a 9 T PPMS (Physical Properties Measurement System, Quantum Design) at temperatures ranging from 10 to 300 K at a cooling/warming rate of 3 K/min.

Spectroscopic Ellipsometry Measurements. Spectroscopic ellipsometry measurements are conducted using a custom-made Variable Angle Spectroscopic Ellipsometer (VASE, J.A. Woollam Co., Inc.) with the photon energy range 0.60−4.80 eV at an incident angle of 70° with respect to the plane normal. Ellipsometry parameters Ψ (the ratio between the amplitude of p and s-polarized reflected light) and Δ (the phase difference between p and s-polarized reflected light) in a high-vacuum chamber with a base pressure of 1×10^{-9} mbar at the respective temperature. The substrate layers (bulk LAO, LSAT, or STO) have also been measured under the same conditions. The optical conductivity, σ_1, of the respective NNO thin-film layers has been extracted from parameters Ψ and Δ utilizing an air/NNO/substrate multilayer model, where the NNO film comprises a homogeneously uniform medium and a composite heterointerface component.

X-ray Absorption Spectroscopy. The O *K*-edge absorption spectra in the energy range 520−580 eV and Ni *L*-edge absorption spectra in the energy range 845−880 eV were obtained using linearly polarized X-ray absorption spectroscopy at the Surface, Interface and Nanostructure Science (SINS) beamline at Singapore Synchrotron Light Source (SSLS), using the Total Electron Yield detection mode. The experiment was conducted in an ultrahigh-vacuum chamber with a base pressure of 1×10^{-10} mbar. The spectra were normalized to the integrated intensity between 565 and 580 eV for the O *K*-edge spectra and between 870 and 880 eV for the Ni *L*-edge spectra, where the tail end of the spectra is located.

DFT. The first-principles calculations were performed with the DFT as implemented in the SIESTA code.[76,77] We use the PBEsol functional, which is optimized for predicting the structures of solid structures. The pseudopotentials are from the Pseudodojo data set.[78] A Hubbard *U* correction[79] is used to get better description of the Ni 3d electronic structure, with an U(Ni) = 2 eV. We use a double-ζ-polarized basis set for the electron wave function. The *k*-point mesh is set to $6 \times 6 \times 1$ for the heterostructure. A structure with 4 uc of NNO and 4 uc of STO, with NdO-TiO_2 layers at the interface, and a vacuum layer of 20 Å at both ends. In each layer, a $\sqrt{2} \times \sqrt{2}$-unit cell structure is taken so that the rotations and the breathing distortions of the oxygen octahedra are allowed. A ferromagnetic spin configuration is assumed in the NNO structure instead of the ground state of the S-type antiferromagnetic structure to reduce the computational complexity. The in-plane lattice parameters are constrained to those of the substrate (3.905 Å for STO). The structures are relaxed until the forces are less than 310^{-3} eV/Å, and the stresses are less than 1 GPa.

ASSOCIATED CONTENT

Data Availability Statement

The data that support the findings of this study are available from the corresponding author upon reasonable request.

Supporting Information

The Supporting Information is available free of charge at https://pubs.acs.org/doi/10.1021/acsnano.4c09921.

Detailed methodology and analysis of the spectroscopic ellipsometry data, complementary X-ray absorption spectroscopic and transport measurement data, and additional DFT calculations (PDF)

AUTHOR INFORMATION

Corresponding Authors

Chi Sin Tang − *Shanghai Key Laboratory of High Temperature Superconductors, Department of Physics, Shanghai University, Shanghai 200444, China; Singapore Synchrotron Light Source (SSLS), National University of Singapore, Singapore 117603, Singapore;* orcid.org/0000-0002-2414-7192; Email: slscst@nus.edu.sg

Le Wang − *Physical and Computational Sciences Directorate, Pacific Northwest National Laboratory, Richland, Washington 99354, United States;* orcid.org/0000-0002-7730-9482; Email: le.wang@pnnl.gov

https://doi.org/10.1021/acsnano.4c09921
ACS Nano 2024, 18, 27707−27717

Xinmao Yin − *Shanghai Key Laboratory of High Temperature Superconductors, Department of Physics, Shanghai University, Shanghai 200444, China;* orcid.org/0000-0002-8246-4444; Email: yinxinmao@shu.edu.cn

Authors

Mingyao Chen − *Shanghai Key Laboratory of High Temperature Superconductors, Department of Physics, Shanghai University, Shanghai 200444, China*

Huimin Liu − *Shanghai Key Laboratory of High Temperature Superconductors, Department of Physics, Shanghai University, Shanghai 200444, China*

Xu He − *Theoretical Materials Physics, Q-MAT, CESAM, Université de Liège, Liège B-4000, Belgium*

Minjuan Li − *Shanghai Key Laboratory of High Temperature Superconductors, Department of Physics, Shanghai University, Shanghai 200444, China*

Mengxia Sun − *Shanghai Key Laboratory of High Temperature Superconductors, Department of Physics, Shanghai University, Shanghai 200444, China;* orcid.org/0009-0004-8867-2297

Krishna Prasad Koirala − *Physical and Computational Sciences Directorate, Pacific Northwest National Laboratory, Richland, Washington 99354, United States*

Mark E. Bowden − *Physical and Computational Sciences Directorate, Pacific Northwest National Laboratory, Richland, Washington 99354, United States;* orcid.org/0000-0003-3812-3340

Yangyang Li − *School of Physics, Shandong University, Jinan, Shandong 250100, China;* orcid.org/0000-0003-4469-0659

Xiongfang Liu − *Shanghai Key Laboratory of High Temperature Superconductors, Department of Physics, Shanghai University, Shanghai 200444, China*

Difan Zhou − *Shanghai Key Laboratory of High Temperature Superconductors, Department of Physics, Shanghai University, Shanghai 200444, China*

Shuo Sun − *Shanghai Key Laboratory of High Temperature Superconductors, Department of Physics, Shanghai University, Shanghai 200444, China;* orcid.org/0000-0001-6092-7148

Mark B.H. Breese − *Singapore Synchrotron Light Source (SSLS), National University of Singapore, Singapore 117603, Singapore; Department of Physics, Faculty of Science, National University of Singapore, Singapore 117542, Singapore*

Chuanbing Cai − *Shanghai Key Laboratory of High Temperature Superconductors, Department of Physics, Shanghai University, Shanghai 200444, China*

Yingge Du − *Physical and Computational Sciences Directorate, Pacific Northwest National Laboratory, Richland, Washington 99354, United States;* orcid.org/0000-0001-9680-1950

Andrew T. S. Wee − *Department of Physics, Faculty of Science, National University of Singapore, Singapore 117542, Singapore; Centre for Advanced 2D Materials and Graphene Research, National University of Singapore, Singapore 117546, Singapore;* orcid.org/0000-0002-5828-4312

Complete contact information is available at: https://pubs.acs.org/10.1021/acsnano.4c09921

Author Contributions

X.Y. conceived the project. L.W. synthesized the thin films. Y.L. conducted the in-plane transport experiments, and L.W. performed the data analysis. M.E.B. carried out the XRD measurements. K.P.K. conducted the STEM measurements and data analysis under the supervision of Y.D. C.S.T. performed the XAS experiments, and M.C. analyzed the data. M.S., C.S.T., X.L., and H.L. performed the SE experiments and analyzed the data. X.H. did the DFT simulations. M.C., C.S.T., X.H., L.W., and X.Y. wrote the manuscript, with input from all the authors.

Notes

The authors declare no competing financial interest.

ACKNOWLEDGMENTS

The authors would like to acknowledge the Singapore Synchrotron Light Source for providing the facility necessary for conducting the research. The Laboratory is a National Research Infrastructure under the National Research Foundation, Singapore. Any opinions, findings, and conclusions or recommendations expressed in this material are those of the authors and do not reflect the views of National Research Foundation, Singapore. This work was supported by the National Natural Science Foundation of China (Grant Nos. 52172271, 12374378, and 52307026); the National Key R&D Program of China (Grant No. 2022YFE03150200); Shanghai Science and Technology Innovation Program (Grant No. 22511100200); and the Strategic Priority Research Program of the Chinese Academy of Sciences (Grant No. XDB25000000). XRD and STEM measurements along with the corresponding analysis and manuscript writing were supported by the U.S. Department of Energy (DOE), Office of Science, Basic Energy Sciences, Division of Materials Sciences and Engineering, Synthesis and Processing Science Program, under Award #10122. C.S.T acknowledges the support from the NUS Emerging Scientist Fellowship. X.H. acknowledges the financial support from F.R.S.-FNRS Belgium through the PDR project PROMOSPAN (Grant No. T.0107.20).

REFERENCES

(1) Han, S.; Tang, C. S.; Li, L.; Liu, Y.; Liu, H.; Gou, J.; Wu, J.; Zhou, D.; Yang, P.; Diao, C.; Ji, J.; Bao, J.; Zhang, L.; Zhao, M.; Milošević, M. V.; Guo, Y.; Tian, L.; Breese, M. B. H.; Cao, G.; Cai, C.; Wee, A. T. S.; Yin, X. Orbital-Hybridization-Driven Charge Density Wave Transition in CsV3Sb5 Kagome Superconductor. *Adv. Mater.* **2023**, *35* (8), No. e2209010.

(2) Yin, X.; Tang, C. S.; Zeng, S.; Asmara, T. C.; Yang, P.; Naradipa, M. A.; Trevisanutto, P. E.; Shirakawa, T.; Kim, B. H.; Yunoki, S.; Breese, M. B. H.; Venkatesan, T.; Wee, A. T. S.; Ariando, A.; Rusydi, A. Quantum Correlated Plasmons and Their Tunability in Undoped and Doped Mott-Insulator Cuprates. *ACS Photonics* **2019**, *6* (12), 3281−3289.

(3) Liu, C.; Yan, X.; Jin, D.; Ma, Y.; Hsiao, H.-W.; Lin, Y.; Bretz-Sullivan, T. M.; Zhou, X.; Pearson, J.; Fisher, B.; Jiang, J. S.; Han, W.; Zuo, J.-M.; Wen, J.; Fong, D. D.; Sun, J.; Zhou, H.; Bhattacharya, A. Two-dimensional superconductivity and anisotropic transport at KTaO3 (111) interfaces. *Science* **2021**, *371* (6530), 716−721.

(4) Ren, T.; Li, M.; Sun, X.; Ju, L.; Liu, Y.; Hong, S.; Sun, Y.; Tao, Q.; Zhou, Y.; Xu, Z.-A.; Xie, Y. Two-dimensional superconductivity at the surfaces of KTaO3 gated with ionic liquid. *Sci. Adv.* **2022**, *8* (22), No. eabn4273.

(5) Liu, T.; Shen, L.; Cheng, S. D.; Wang, H.; Li, Y.; Liu, M. Interfacial Modulation on Co(0.2)Fe(2.8)O(4) Epitaxial Thin Films for Anomalous Hall Sensor Applications. *ACS Appl. Mater. Interfaces* **2022**, *14* (33), 37887−37893.

(6) Lim, S.-M.; Yeon, H.-W.; Lee, G.-B.; Jin, M.-G.; Lee, S.-Y.; Jo, J.; Kim, M.; Joo, Y.-C. Thermally Stable Amorphous Oxide-based Schottky Diodes through Oxygen Vacancy Control at Metal/Oxide Interfaces. *Sci. Rep.* **2019**, *9* (1), 7872.
(7) Grisolia, M. N.; Varignon, J.; Sanchez-Santolino, G.; Arora, A.; Valencia, S.; Varela, M.; Abrudan, R.; Weschke, E.; Schierle, E.; Rault, J. E.; Rueff, J. P.; Barthelemy, A.; Santamaria, J.; Bibes, M. Hybridization-controlled charge transfer and induced magnetism at correlated oxide interfaces. *Nat. Phys.* **2016**, *12* (5), 484−492.
(8) Wang, L.; Yang, Z.; Bowden, M. E.; Freeland, J. W.; Sushko, P. V.; Spurgeon, S. R.; Matthews, B.; Samarakoon, W. S.; Zhou, H.; Feng, Z.; Engelhard, M. H.; Du, Y.; Chambers, S. A. Hole-Trapping-Induced Stabilization of Ni4 + in SrNiO3/LaFeO3 Superlattices. *Adv. Mater.* **2020**, *32* (45), No. e2005003.
(9) Li, Y.; Hou, P.; Xi, Z.; Xu, Y.; Liu, Y.; Tian, H.; Li, J.; Yang, Y.; Deng, Y.; Wu, D. Charge transfer driving interfacial reconstructions in perovskite oxide heterostructures. *Commun. Phys.* **2023**, *6* (1), 70.
(10) Tang, C. S.; Yin, X.; Zeng, S.; Wu, J.; Yang, M.; Yang, P.; Diao, C.; Feng, Y. P.; Breese, M. B. H.; Chia, E. E. M.; Venkatesan, T.; Chhowalla, M.; Ariando, A.; Rusydi, A.; Wee, A. T. S. Interfacial Oxygen-Driven Charge Localization and Plasmon Excitation in Unconventional Superconductors. *Adv. Mater.* **2020**, *32* (34), No. e2000153.
(11) Chen, X.; Zhang, S.; Liu, B.; Hu, F.; Shen, B.; Sun, J. Theoretical investigation of magnetic anisotropy at the La0.5Sr0.5MnO3/LaCoO2.5 interface. *Phys. Rev. B* **2019**, *100* (14), No. 144413.
(12) Liao, Z.; Gauquelin, N.; Green, R. J.; Macke, S.; Gonnissen, J.; Thomas, S.; Zhong, Z.; Li, L.; Si, L.; Van Aert, S.; Hansmann, P.; Held, K.; Xia, J.; Verbeeck, J.; Van Tendeloo, G.; Sawatzky, G. A.; Koster, G.; Huijben, M.; Rijnders, G. Thickness Dependent Properties in Oxide Heterostructures Driven by Structurally Induced Metal−Oxygen Hybridization Variations. *Adv. Funct. Mater.* **2017**, *27* (17), No. 1606717.
(13) Nichols, J.; Gao, X.; Lee, S.; Meyer, T. L.; Freeland, J. W.; Lauter, V.; Yi, D.; Liu, J.; Haskel, D.; Petrie, J. R.; Guo, E.-J.; Herklotz, A.; Lee, D.; Ward, T. Z.; Eres, G.; Fitzsimmons, M. R.; Lee, H. N. Emerging magnetism and anomalous Hall effect in iridate-Manganite heterostructures. *Nat. Commun.* **2016**, *7*, No. 12721.
(14) Yi, D.; Liu, J.; Hsu, S. L.; Zhang, L.; Choi, Y.; Kim, J. W.; Chen, Z.; Clarkson, J. D.; Serrao, C. R.; Arenholz, E.; Ryan, P. J.; Xu, H.; Birgeneau, R. J.; Ramesh, R. Atomic-scale control of magnetic anisotropy via novel spin-orbit coupling effect in La2/3Sr1/3MnO3/SrIrO3 superlattices. *Proc. Natl. Acad. Sci. U. S. A.* **2016**, *113* (23), 6397−402.
(15) Liao, Z.; Huijben, M.; Zhong, Z.; Gauquelin, N.; Macke, S.; Green, R. J.; Van Aert, S.; Verbeeck, J.; Van Tendeloo, G.; Held, K.; Sawatzky, G. A.; Koster, G.; Rijnders, G. Controlled lateral anisotropy in correlated Manganite heterostructures by interface-engineered oxygen octahedral coupling. *Nat. Mater.* **2016**, *15* (4), 425−31.
(16) Zhang, P.; Das, A.; van Rijn, J. J. L.; Watson, A. J.; Banerjee, T. Tunable magnetic anisotropy in SrMnO3/SrRuO3 bilayers studied by angle and temperature dependence of magneto-transport. *Appl. Phys. Lett.* **2022**, *121* (15), 152401.
(17) Gibert, M.; Zubko, P.; Scherwitzl, R.; Iniguez, J.; Triscone, J.-M. Exchange bias in LaNiO3-LaMnO3 superlattices. *NATURE MATERIALS* **2012**, *11* (3), 195−198.
(18) Sanchez-Manzano, D.; Mesoraca, S.; Cuellar, F. A.; Cabero, M.; Rouco, V.; Orfila, G.; Palermo, X.; Balan, A.; Marcano, L.; Sander, A.; Rocci, M.; Garcia-Barriocanal, J.; Gallego, F.; Tornos, J.; Rivera, A.; Mompean, F.; Garcia-Hernandez, M.; Gonzalez-Calbet, J. M.; Leon, C.; Valencia, S.; Feuillet-Palma, C.; Bergeal, N.; Buzdin, A. I.; Lesueur, J.; Villegas, J. E.; Santamaria, J. Extremely long-range, high-temperature Josephson coupling across a half-metallic ferromagnet. *Nat. Mater.* **2022**, *21* (2), 188.
(19) Singh, S.; Basu, S. Investigation of interface magnetism of complex oxide heterostructures using polarized neutron reflectivity. *CURRENT APPLIED PHYSICS* **2017**, *17* (5), 615−625.
(20) Ren, Z.; Wu, M.; Chen, X.; Li, W.; Li, M.; Wang, F.; Tian, H.; Chen, J.; Xie, Y.; Mai, J.; Li, X.; Lu, X.; Lu, Y.; Zhang, H.; Van Tendeloo, G.; Zhang, Z.; Han, G. Electrostatic Force-Driven Oxide Heteroepitaxy for Interface Control. *Adv. Mater.* **2018**, *30* (38), No. 1707017.
(21) Flint, C. L.; Jang, H.; Lee, J.-S.; N'Diaye, A. T.; Shafer, P.; Arenholz, E.; Suzuki, Y. Role of polar compensation in interfacial ferromagnetism of LaNiO3/CaMnO3 superlattices. *Phys. Rev. Mater.* **2017**, *1* (2), No. 024404.
(22) Chen, H.; Millis, A. Charge transfer driven emergent phenomena in oxide heterostructures. *J. Phys.: Condens. Matter* **2017**, *29* (24), 243001.
(23) Chakhalian, J.; Freeland, J. W.; Habermeier, H. U.; Cristiani, G.; Khaliullin, G.; van Veenendaal, M.; Keimer, B. Orbital reconstruction and covalent bonding at an oxide interface. *Science* **2007**, *318* (5853), 1114−7.
(24) Bert, J. A.; Kalisky, B.; Bell, C.; Kim, M.; Hikita, Y.; Hwang, H. Y.; Moler, K. A. Direct imaging of the coexistence of ferromagnetism and superconductivity at the LaAlO3/SrTiO3 interface. *Nat. Phys.* **2011**, *7* (10), 767−771.
(25) Li, D.; Lee, K.; Wang, B. Y.; Osada, M.; Crossley, S.; Lee, H. R.; Cui, Y.; Hikita, Y.; Hwang, H. Y. Superconductivity in an infinite-layer nickelate. *Nature* **2019**, *572* (7771), 624−627.
(26) Sakakibara, H.; Usui, H.; Suzuki, K.; Kotani, T.; Aoki, H.; Kuroki, K. Model Construction and a Possibility of Cupratelike Pairing in a New d(9) Nickelate Superconductor (Nd,Sr)NiO2. *Phys. Rev. Mater.* **2020**, *125* (7), No. 077003.
(27) Hepting, M.; Li, D.; Jia, C. J.; Lu, H.; Paris, E.; Tseng, Y.; Feng, X.; Osada, M.; Been, E.; Hikita, Y.; Chuang, Y.-D.; Hussain, Z.; Zhou, K. J.; Nag, A.; Garcia-Fernandez, M.; Rossi, M.; Huang, H. Y.; Huang, D. J.; Shen, Z. X.; Schmitt, T.; Hwang, H. Y.; Moritz, B.; Zaanen, J.; Devereaux, T. P.; Lee, W. S. Electronic structure of the parent compound of superconducting infinite-layer nickelates. *Nat. Mater.* **2020**, *19* (4), 381.
(28) Middey, S.; Chakhalian, J.; Mahadevan, P.; Freeland, J. W.; Millis, A. J.; Sarma, D. D. Physics of Ultrathin Films and Heterostructures of Rare-Earth Nickelates. *Annu. Rev. Mater. Res.* **2016**, *46* (1), 305−334.
(29) Wang, L.; Stoerzinger, K. A.; Chang, L.; Zhao, J.; Li, Y.; Tang, C. S.; Yin, X.; Bowden, M. E.; Yang, Z.; Guo, H.; You, L.; Guo, R.; Wang, J.; Ibrahim, K.; Chen, J.; Rusydi, A.; Wang, J.; Chambers, S. A.; Du, Y. Tuning Bifunctional Oxygen Electrocatalysts by Changing the A-Site Rare-Earth Element in Perovskite Nickelates. *Adv. Funct. Mater.* **2018**, *28* (39), No. 1803712.
(30) Catalano, S.; Gibert, M.; Fowlie, J.; Íñiguez, J.; Triscone, J. M.; Kreisel, J. Rare-earth nickelates RNiO3: thin films and heterostructures. *Rep. Prog. Phys.* **2018**, *81* (4), No. 046501.
(31) Wang, L.; Zhang, Q.; Chang, L.; You, L.; He, X.; Jin, K.; Gu, L.; Guo, H.; Ge, C.; Feng, Y.; Wang, J. Electrochemically Driven Giant Resistive Switching in Perovskite Nickelates Heterostructures. *Adv. Electron. Mater.* **2017**, *3* (10), No. 1700321.
(32) Gogoi, P. K.; Sponza, L.; Schmidt, D.; Asmara, T. C.; Diao, C.; Lim, J. C. W.; Poh, S. M.; Kimura, S.-i.; Trevisanutto, P. E.; Olevano, V.; Rusydi, A. Anomalous excitons and screenings unveiling strong electronic correlations in ${\mathrm{SrTi}}_{1\ensuremath{-}x}-{\mathrm{Nb}}_{x}{\mathrm{O}}_{3} (0\ensuremath{\le}x\ensuremath{\le}0.005)$. *Phys. Rev. B* **2015**, *92* (3), No. 035119.
(33) Gogoi, P. K.; Trevisanutto, P. E.; Yang, M.; Santoso, I.; Asmara, T. C.; Terentjevs, A.; Della Sala, F.; Breese, M. B. H.; Venkatesan, T.; Feng, Y. P.; Loh, K. P.; Neto, A. H. C.; Rusydi, A. Optical conductivity renormalization of graphene on $\mathrm{SrTiO}{}_{3}$ due to resonant excitonic effects mediated by Ti $3d$ orbitals. *Phys. Rev. B* **2015**, *91* (3), No. 035424.
(34) Yin, X.; Tang, C. S.; Majidi, M. A.; Ren, P.; Wang, L.; Yang, P.; Diao, C.; Yu, X.; Breese, M. B. H.; Wee, A. T. S.; Wang, J.; Rusydi, A. Modulation of Manganite Nanofilm Properties Mediated by Strong Influence of Strontium Titanate Excitons. *ACS Appl. Mater. Interfaces* **2018**, *10* (41), 35563−35570.
(35) Yin, X.; Yang, M.; Tang, C. S.; Wang, Q.; Xu, L.; Wu, J.; Trevisanutto, P. E.; Zeng, S.; Chin, X. Y.; Asmara, T. C.; Feng, Y. P.; Ariando, A.; Chhowalla, M.; Wang, S. J.; Zhang, W.; Rusydi, A.; Wee,

https://doi.org/10.1021/acsnano.4c09921
ACS Nano 2024, 18, 27707−27717

A. T. S. Modulation of New Excitons in Transition Metal Dichalcogenide-Perovskite Oxide System. *Adv. Sci.* **2019**, *6* (12), No. 1900446.
(36) Tang, C. S.; Yin, X.; Zeng, S.; Wu, J.; Yang, M.; Yang, P.; Diao, C.; Feng, Y. P.; Breese, M. B. H.; Chia, E. E. M.; Venkatesan, T.; Chhowalla, M.; Ariando, A.; Rusydi, A.; Wee, A. T. S. Interfacial Oxygen-Driven Charge Localization and Plasmon Excitation in Unconventional Superconductors. *Adv. Mater.* **2020**, *32* (34), No. 2000153.
(37) Zaanen, J.; Sawatzky, G. A.; Allen, J. W. Band gaps and electronic structure of transition-metal compounds. *Phys. Rev. Lett.* **1985**, *55* (4), 418−421.
(38) Zeng, S. W.; Yin, X. M.; Li, C. J.; Chow, L. E.; Tang, C. S.; Han, K.; Huang, Z.; Cao, Y.; Wan, D. Y.; Zhang, Z. T.; Lim, Z. S.; Diao, C. Z.; Yang, P.; Wee, A. T. S.; Pennycook, S. J.; Ariando, A. Observation of perfect diamagnetism and interfacial effect on the electronic structures in infinite layer Nd0.8Sr0.2NiO2 superconductors. *Nat. Commun.* **2022**, *13* (1), 743.
(39) Zhang, Y.; Lin, L.-F.; Hu, W.; Moreo, A.; Dong, S.; Dagotto, E. Similarities and differences between nickelate and cuprate films grown on a ${\mathrm{SrTiO}}_{3}$ substrate. *Phys. Rev. B* **2020**, *102* (19), No. 195117.
(40) Geisler, B.; Pentcheva, R. Fundamental difference in the electronic reconstruction of infinite-layer versus perovskite neodymium nickelate films on SrTiO3(001). *Phys. Rev. B* **2020**, *102* (2), No. 020502.
(41) He, R.; Jiang, P.; Lu, Y.; Song, Y.; Chen, M.; Jin, M.; Shui, L.; Zhong, Z. Polarity-induced electronic and atomic reconstruction at NdNiO2/SrTiO3 interfaces. *Phys. Rev. B* **2020**, *102* (3), No. 035118.
(42) Bernardini, F.; Cano, A. Stability and electronic properties of LaNiO2/SrTiO(3)heterostructures. *J. Phys.: Mater.* **2020**, *3* (3), No. 03LT01.
(43) Peng, J. J.; Song, C.; Wang, M.; Li, F.; Cui, B.; Wang, G. Y.; Yu, P.; Pan, F. Manipulating the metal-to-insulator transition ofNdNiO3-films by orbital polarization. *Phys. Rev. B* **2016**, *93* (23), No. 235102.
(44) Disa, A. S.; Kumah, D. P.; Ngai, J. H.; Specht, E. D.; Arena, D. A.; Walker, F. J.; Ahn, C. H. Phase diagram of compressively strained nickelate thin films. *APL Mater.* **2013**, *1* (3), No. 032110.
(45) Goodge, B. H.; Geisler, B.; Lee, K.; Osada, M.; Wang, B. Y.; Li, D.; Hwang, H. Y.; Pentcheva, R.; Kourkoutis, L. F. Resolving the polar interface of infinite-layer nickelate thin films. *Nat. Mater.* **2023**, *22* (4), 466−473.
(46) Wang, L.; Stoerzinger, K. A.; Chang, L.; Yin, X.; Li, Y.; Tang, C. S.; Jia, E.; Bowden, M. E.; Yang, Z.; Abdelsamie, A.; You, L.; Guo, R.; Chen, J.; Rusydi, A.; Wang, J.; Chambers, S. A.; Du, Y. Strain Effect on Oxygen Evolution Reaction Activity of Epitaxial NdNiO(3) Thin Films. *ACS Appl. Mater. Interfaces* **2019**, *11* (13), 12941−12947.
(47) Chandrasena, R. U.; Yang, W.; Lei, Q.; Delgado-Jaime, M. U.; Wijesekara, K. D.; Golalikhani, M.; Davidson, B. A.; Arenholz, E.; Kobayashi, K.; Kobata, M.; de Groot, F. M. F.; Aschauer, U.; Spaldin, N. A.; Xi, X.; Gray, A. X. Strain-Engineered Oxygen Vacancies in CaMnO3 Thin Films. *Nano Lett.* **2017**, *17* (2), 794−799.
(48) Petrie, J. R.; Jeen, H.; Barron, S. C.; Meyer, T. L.; Lee, H. N. Enhancing Perovskite Electrocatalysis through Strain Tuning of the Oxygen Deficiency. *J. Am. Chem. Soc.* **2016**, *138* (23), 7252−7255.
(49) Stewart, M. K.; Liu, J.; Kareev, M.; Chakhalian, J.; Basov, D. N. Mott Physics near the Insulator-To-Metal Transition in NdNiO3. *Phys. Rev. Lett.* **2011**, *107* (17), No. 176401.
(50) Chang, L.; Wang, L.; You, L.; Yang, Z.; Abdelsamie, A.; Zhang, Q.; Zhou, Y.; Gu, L.; Chambers, S. A.; Wang, J. Tuning Photovoltaic Performance of Perovskite Nickelates Heterostructures by Changing the A-Site Rare-Earth Element. *ACS Appl. Mater. Interfaces* **2019**, *11* (17), 16191−16197.
(51) Stewart, M. K.; Brownstead, D.; Liu, J.; Kareev, M.; Chakhalian, J.; Basov, D. N. Heterostructuring and strain effects on the infrared optical properties of nickelates. *Phys. Rev. B* **2012**, *86* (20), No. 205102.
(52) Stewart, M. K.; Liu, J.; Kareev, M.; Chakhalian, J.; Basov, D. N. Mott Physics near the Insulator-To-Metal Transition in ${\mathrm{NdNiO}}_{3}$. *Phys. Rev. Lett.* **2011**, *107* (17), No. 176401.
(53) Ruppen, J.; Teyssier, J.; Ardizzone, I.; Peil, O. E.; Catalano, S.; Gibert, M.; Triscone, J. M.; Georges, A.; van der Marel, D. Impact of antiferromagnetism on the optical properties of rare-earth nickelates. *Phys. Rev. B* **2017**, *96* (4), No. 045120.
(54) Ruppen, J.; Teyssier, J.; Peil, O. E.; Catalano, S.; Gibert, M.; Mravlje, J.; Triscone, J. M.; Georges, A.; van der Marel, D. Optical spectroscopy and the nature of the insulating state of rare-earth nickelates. *Phys. Rev. B* **2015**, *92* (15), No. 155145.
(55) Yin, X.; Majidi, M. A.; Chi, X.; Ren, P.; You, L.; Palina, N.; Yu, X.; Diao, C.; Schmidt, D.; Wang, B.; Yang, P.; Breese, M. B. H.; Wang, J.; Rusydi, A. Unraveling how electronic and spin structures control macroscopic properties of Manganite ultra-thin films. *NPG Asia Materials* **2015**, *7* (7), e196−e196.
(56) Rusydi, A.; Rauer, R.; Neuber, G.; Bastjan, M.; Mahns, I.; Müller, S.; Saichu, P.; Schulz, B.; Singer, S. G.; Lichtenstein, A. I.; Qi, D.; Gao, X.; Yu, X.; Wee, A. T. S.; Stryganyuk, G.; Dörr, K.; Sawatzky, G. A.; Cooper, S. L.; Rübhausen, M. Metal-insulator transition in manganites: Changes in optical conductivity up to 22 eV. *Phys. Rev. B* **2008**, *78* (12), No. 125110.
(57) Ruppen, J.; Teyssier, J.; Ardizzone, I.; Peil, O. E.; Catalano, S.; Gibert, M.; Triscone, J. M.; Georges, A.; van der Marel, D. Impact of antiferromagnetism on the optical properties of rare earth nickelates. *Phys. Rev. B* **2017**, *96* (4), No. 045120.
(58) Trevisanutto, P. E.; Olevano, V.; Rusydi, A.; Gogoi, P. K.; Sponza, L.; Schmidt, D.; Asmara, T. C.; Diao, C.; Lim, J. C. W.; Poh, S. M.; Kimura, S.-i Anomalous excitons and screenings unveiling strong electronic correlations inSrTi1−xNbxO3 ($0 \leq x \leq 0.005$). *Phys. Rev. B* **2015**, *92* (3), No. 035119.
(59) Goodge, B. H.; Li, D.; Lee, K.; Osada, M.; Wang, B. Y.; Sawatzky, G. A.; Hwang, H. Y.; Kourkoutis, L. F. Doping evolution of the Mott-Hubbard landscape in infinite-layer nickelates. *Proc. Natl. Acad. Sci. U. S. A.* **2021**, *118* (2), No. e2007683118.
(60) Liu, J.; Kargarian, M.; Kareev, M.; Gray, B.; Ryan, P. J.; Cruz, A.; Tahir, N.; Chuang, Y.-D.; Guo, J.; Rondinelli, J. M.; Freeland, J. W.; Fiete, G. A.; Chakhalian, J. Heterointerface engineered electronic and magnetic phases of NdNiO3 thin films. *Nat. Commun.* **2013**, *4*, 2714.
(61) Palina, N.; Wang, L.; Dash, S.; Yu, X.; Breese, M. B. H.; Wang, J.; Rusydi, A. Investigation of the metal-insulator transition in NdNiO(3) films by site-selective X-ray absorption spectroscopy. *Nanoscale* **2017**, *9* (18), 6094−6102.
(62) Wang, L.; Yang, Z.; Yin, X.; Taylor, S. D.; He, X.; Tang, C. S.; Bowden, M. E.; Zhao, J.; Wang, J.; Liu, J.; Perea, D. E.; Wangoh, L.; Wee, A. T. S.; Zhou, H.; Chambers, S. A.; Du, Y. Spontaneous phase segregation of Sr2NiO3 and SrNi2O3 during SrNiO3 heteroepitaxy. *Sci. Adv.* **2021**, *7* (10), No. eabe2866.
(63) Mundet, B.; Domínguez, C.; Fowlie, J.; Gibert, M.; Triscone, J.-M.; Alexander, D. T. L. Near-Atomic-Scale Mapping of Electronic Phases in Rare Earth Nickelate Superlattices. *Nano Lett.* **2021**, *21* (6), 2436−2443.
(64) Lee, J.; Kim, G.-Y.; Jeong, S.; Yang, M.; Kim, J.-W.; Cho, B.-G.; Choi, Y.; Kim, S.; Choi, J. S.; Lee, T. K.; Kim, J.; Lee, D. R.; Chang, S. H.; Park, S.; Jung, J. H.; Bark, C. W.; Koo, T.-Y.; Ryan, P. J.; Ihm, K.; Kim, S.; Choi, S.-Y.; Kim, T. H.; Lee, S. Template Engineering of Metal-to-Insulator Transitions in Epitaxial Bilayer Nickelate Thin Films. *ACS APPLIED MATERIALS & INTERFACES* **2021**, *13* (45), 54466−54475.
(65) Liu, J.; Kareev, M.; Meyers, D.; Gray, B.; Ryan, P.; Freeland, J. W.; Chakhalian, J. Metal-Insulator Transition and Orbital Reconstruction in Mott-Type Quantum Wells Made of NdNiO3. *Phys. Rev. Lett.* **2012**, *109* (10), No. 107402.
(66) Freeland, J. W.; van Veenendaal, M.; Chakhalian, J. Evolution of electronic structure across the rare-earth RNiO3 series. *J. Electron Spectrosc. Relat. Phenom.* **2016**, *208*, 56−62.
(67) Bodenthin, Y.; Staub, U.; Piamonteze, C.; Garcia-Fernandez, M.; Martinez-Lope, M. J.; Alonso, J. A. Magnetic and electronic

https://doi.org/10.1021/acsnano.4c09921
ACS Nano 2024, 18, 27707−27717

properties of RNiO3 (R = Pr, Nd, Eu, Ho and Y) perovskites studied by resonant soft x-ray magnetic powder diffraction. *J. Phys.: Condens. Matter* **2011**, *23* (3), No. 036002.
(68) Gauquelin, N.; Benckiser, E.; Kinyanjui, M. K.; Wu, M.; Lu, Y.; Christiani, G.; Logvenov, G.; Habermeier, H.-U.; Kaiser, U.; Keimer, B.; Botton, G. A. Atomically resolved EELS mapping of the interfacial structure of epitaxially strained LaNiO3/LaAlO3 superlattices. *Phys. Rev. B* **2014**, *90* (19), No. 195140.
(69) Tang, C. S.; Yin, X.; Yang, M.; Wu, D.; Birowosuto, M. D.; Wu, J.; Li, C.; Hettiarachchi, C.; Chin, X. Y.; Chang, Y. H.; Ouyang, F.; Dang, C.; Pennycook, S. J.; Feng, Y. P.; Wang, S.; Chi, D.; Breese, M. B. H.; Zhang, W.; Rusydi, A.; Wee, A. T. S. Three-Dimensional Resonant Exciton in Monolayer Tungsten Diselenide Actuated by Spin-Orbit Coupling. *ACS Nano* **2019**, *13* (12), 14529−14539.
(70) Kresse, G.; Furthmüller, J. Efficiency of ab-initio total energy calculations for metals and semiconductors using a plane-wave basis set. *Comput. Mater. Sci.* **1996**, *6*, 15−50.
(71) Kresse, G.; Furthmüller, J. Efficient iterative schemes for ab initio total-energy calculations using a plane-wave basis set. *Phys. Rev. B* **1996**, *54*, 11169−11186.
(72) Kresse, G.; Hafner, J. Ab initio molecular dynamics for liquid metals. *Phys. Rev. B* **1993**, *47*, 558−561.
(73) Kresse, G.; Hafner, J. Ab initio molecular-dynamics simulation of the liquid-metal —amorphous-semiconductor transition in germanium. *Phys. Rev. B* **1994**, *49*, 14251−14269.
(74) Park, H.; Millis, A. J.; Marianetti, C. A. Site-Selective Mott Transition in Rare-Earth-Element Nickelates. *Phys. Rev. Lett.* **2012**, *109* (15), No. 156402.
(75) Varignon, J.; Grisolia, M. N.; Íñiguez, J.; Barthélémy, A.; Bibes, M. Complete phase diagram of rare-earth nickelates from first-principles. *npj Quantum Mater.* **2017**, *2* (1), 21.
(76) José, M. S.; Emilio, A.; Julian, D. G.; Alberto, G.; Javier, J.; Pablo, O.; Daniel, S.-P. The SIESTA method for ab initio order-N materials simulation. *J. Phys.: Condens. Matter* **2002**, *14* (11), 2745.
(77) García, A.; Papior, N.; Akhtar, A.; Artacho, E.; Blum, V.; Bosoni, E.; Brandimarte, P.; Brandbyge, M.; Cerdá, J. I.; Corsetti, F.; Cuadrado, R.; Dikan, V.; Ferrer, J.; Gale, J.; García-Fernández, P.; García-Suárez, V. M.; García, S.; Huhs, G.; Illera, S.; Korytár, R.; Koval, P.; Lebedeva, I.; Lin, L.; López-Tarifa, P.; Mayo, S. G.; Mohr, S.; Ordejón, P.; Postnikov, A.; Pouillon, Y.; Pruneda, M.; Robles, R.; Sánchez-Portal, D.; Soler, J. M.; Ullah, R.; Yu, V. W.-z.; Junquera, J. Siesta: Recent developments and applications. *J. Chem. Phys.* **2020**, *152* (20), 204108.
(78) van Setten, M. J.; Giantomassi, M.; Bousquet, E.; Verstraete, M. J.; Hamann, D. R.; Gonze, X.; Rignanese, G. M. The PseudoDojo: Training and grading a 85 element optimized norm-conserving pseudopotential table. *Comput. Phys. Commun.* **2018**, *226*, 39−54.
(79) Vladimir, I. A.; Aryasetiawan, F.; Lichtenstein, A. I. First-principles calculations of the electronic structure and spectra of strongly correlated systems: the LDA+ U method. *J. Phys.: Condens. Matter* **1997**, *9* (4), 767.

https://doi.org/10.1021/acsnano.4c09921
ACS Nano 2024, 18, 27707−27717